

Article

Photoluminescence of Chemically and Electrically Doped Two-Dimensional Monolayer Semiconductors

Hyungjin Kim ¹, Valerio Adinolfi ² and Sin-Hyung Lee ^{3,*}¹ Department of Materials Science and Engineering, Yonsei University, Seoul 03722, Republic of Korea² Department of Electrical Engineering and Computer Sciences, University of California, Berkeley, CA 94720, USA; ziofitt@gmail.com³ Department of Intelligent Semiconductor Engineering, School of Advanced Fusion Studies, University of Seoul, Seoul 02504, Republic of Korea

* Correspondence: sinhlee@uos.ac.kr

Abstract: Two-dimensional (2D) transition metal dichalcogenide (TMDC) monolayers exhibit unique physical properties, such as self-terminating surfaces, a direct bandgap, and near-unity photoluminescence (PL) quantum yield (QY), which make them attractive for electronic and optoelectronic applications. Surface charge transfer has been widely used as a technique to control the concentration of free charge in 2D semiconductors, but its estimation and the impact on the optoelectronic properties of the material remain a challenge. In this work, we investigate the optical properties of a WS₂ monolayer under three different doping approaches: benzyl viologen (BV), potassium (K), and electrostatic doping. Owing to the excitonic nature of 2D TMDC monolayers, the PL of the doped WS₂ monolayer exhibits redshift and a decrease in intensity, which is evidenced by the increase in trion population. The electron concentrations of $3.79 \times 10^{13} \text{ cm}^{-2}$, $6.21 \times 10^{13} \text{ cm}^{-2}$, and $3.12 \times 10^{12} \text{ cm}^{-2}$ were measured for WS₂ monolayers doped with BV, K, and electrostatic doping, respectively. PL offers a direct and versatile approach to probe the doping effect, allowing for the measurement of carrier concentration in 2D monolayer semiconductors.

Keywords: photoluminescence; doping; 2D semiconductor; monolayer; TMDC

Citation: Kim, H.; Adinolfi, V.; Lee, S.-H. Photoluminescence of Chemically and Electrically Doped Two-Dimensional Monolayer Semiconductors. *Materials* **2024**, *17*, 3962. <https://doi.org/10.3390/ma17163962>

Academic Editors: Bruno Falcão and Pavani Krishnapuram

Received: 16 July 2024

Revised: 5 August 2024

Accepted: 7 August 2024

Published: 9 August 2024



Copyright: © 2024 by the authors. Licensee MDPI, Basel, Switzerland. This article is an open access article distributed under the terms and conditions of the Creative Commons Attribution (CC BY) license (<https://creativecommons.org/licenses/by/4.0/>).

1. Introduction

Two-dimensional (2D) semiconducting material has attracted great attention over recent years. Its unique properties including self-terminated surfaces, capability of forming van der Waals heterostructures, and layer number-dependent electrical and optical characteristics enabled 2D semiconductors as candidates to be applicable for next-generation optoelectronic and electronic devices [1–5]. In particular, a transition metal dichalcogenide (TMDC), a representative type of 2D semiconducting materials such as MoS₂, WS₂, and WSe₂, exhibits an indirect-to-direct bandgap transition at a monolayer thickness level [6–8]. Despite its peculiar properties, its widespread applications for practical devices have been limited due to a lack of a reliable and controllable doping technique and approach to evaluate the precise doping concentrations and distributions, which are prevalently implemented in conventional complementary metal–oxide–semiconductor (CMOS) technology.

The types of doping strategy for 2D monolayer semiconductors include substitution of atoms, creation of vacancy defects, and surface charge transfer [9–11]. Substitutional doping is performed by replacing the transition metal or chalcogenide atoms in a monolayer semiconductor and tuning the composition between different elements. Although the doping effect can persist as long as the elemental composition is maintained, it is challenging to achieve desirable doping concentration and distribution during synthesis. Unlike in bulk semiconductors, the bombardment of high energy ions onto 2D monolayer semiconductors not only induces doping via vacancy creation but also impairs the materials, thus degrading the performance of monolayer semiconductors because of their

atomically thin nature [12]. Surface charge transfer, on the other hand, induces the doping effect without structural or chemical changes in a monolayer semiconductor. With physical or chemical adsorption of the layer applied, charge carriers migrate from the deposited layer to the adjacent material by diffusion [13–15]. Moreover, the electrostatic field can drive the transport of charge carriers by drift. There have been many approaches and studies on surface charge transfer reported as accessible and efficient methods of doping for 2D monolayer semiconductors [16–20]. However, the surface charge transfer method still involves bottlenecks in the sense that it lacks controllability. In fact, it is demanding to quantify the amount of charge carriers that are transferred to the 2D monolayer semiconductor. Therefore, a systemic approach for determining the effectiveness of surface charge transfer doping on 2D monolayer semiconductors needs to be developed for their practical application, but no such directions have been studied so far.

Recently, recombination physics in 2D TMDC monolayer semiconductors has been explored, which is largely distinct from bulk semiconductors owing to the reduced Coulomb interactions [21–23]. Photoluminescence (PL) quantum yield (QY) is a parameter that is calculated as a ratio of the number of photons emitted to the number of photons absorbed in a material, which is also decided with a relative rate between radiative recombination and nonradiative recombination. PL QY is of significance as a key metric for optoelectronic applications since it directly determines the ultimate efficiency limit that the device can achieve. TMDC monolayers, however, suffer from poor PL QY at room temperature. A number of strategies have been proposed to enhance the low PL QY of TMDC monolayer semiconductors, leading to the demonstration of a near-unity PL QY in monolayer MoS₂ at low exciton generation rates [24–26]. Since neutral exciton recombination is entirely radiative even at high defect densities, the photophysics of 2D TMDC monolayer semiconductors is dictated by the relative population of neutral excitons and trions, which are formed from excitons interacting with background charge carriers [27–29].

In this work, the optical properties of a doped 2D monolayer semiconductor were investigated. Since free carriers form trions to have nonradiative recombination, PL QY of the doped monolayer semiconductor at a certain exciton generation rate offers information on the population of excitons and trions, which the carrier concentration can be extracted from. We further leverage the recombination model of a 2D TMDC monolayer semiconductor to compare and analyze the effect of two surface charge transfer methods: chemical and electrostatic doping. Without perturbing the characteristics of doped 2D monolayer semiconductors, PL promptly reflects the results of doping applied in a monolayer semiconductor. Moreover, it serves as an efficient probe to estimate a wide range of carrier concentration-dependent optical property variations. Our study shows the potential of PL to be employed for characterizing semiconducting materials with various doping conditions even with high defect density.

2. Materials and Methods

WS₂ was mechanically exfoliated from a single crystal source (HQ Graphene, Groningen, The Netherlands) onto a 50 nm SiO₂/p+-Si substrate. Then, monolayers were identified under microscopes with their optical contrast. For a back-gated field-effect transistor (FET), source and drain contacts were patterned via electron beam (e-beam) lithography using PMMA (C4, MicroChem, Austin, TX, USA) as an e-beam resist followed by the e-beam evaporation of Ti/Au (5/25 nm) for electrodes. Electrical measurements were performed with the B1500A semiconductor device parameter analyzer (Keysight, Santa Rosa, CA, USA).

Benzyl viologen (BV) molecules were prepared as a solution for chemical n-doping. Starting with benzyl viologen dichloride (20 mg, Sigma-Aldrich, St. Louis, MO, USA) dissolved in deionized (DI) water and toluene (5 mL/5 mL), the solution was kept for one day after adding sodium borohydride (4 g, Sigma-Aldrich). Doping was performed by extracting and drop-casting the upper layer (toluene) of the bilayer solution onto the sample, followed by N₂ gas to remove the excess molecules and solvents under ambient

conditions. K doping was carried out under vacuum conditions ($\sim 5 \times 10^{-5}$ Torr) inside a home-built chamber where a 5 A current flows through a filament to heat up a boat and K vapor is generated to be evaporated onto the sample for a controlled exposure time. For K doping, a minimum time of 250 s is required to vaporize the K dopants.

Optical measurements were performed in a customized micro-PL setup under ambient conditions (298–300 K, ~ 20 – 30% relative humidity). A laser diode with a 532 nm peak emission wavelength (CNI Laser, Changchun, China) was used as an excitation source and the PL signal was collected with a $50\times$ (NA = 0.55) objective lens (Olympus, Tokyo, Japan) and sent to a spectrometer (DXG) and CCD detector (iDus 420 BEX2-DD, Andor, Abingdon, UK). The detailed calibration procedure of the setup to extract PL QY is provided in previous work [24]. A reference sample (Rhodamine 101, Sigma-Aldrich) of which the PL QY is known was used to confirm the extracted PL QY value and cross-calibrate our setup. For time-resolved PL spectroscopy, the sample was excited by a picosecond (10–20 ps pulse duration) 48 MHz pulsed laser with a 532 nm peak emission wavelength (CNI Laser). The PL signal was detected using a single photon avalanche diode (PDM-50, MPD, Bolzano, Italy) and the time-correlated single photon counting (TCSPC) module (PicoHarp 300, PicoQuant, Berlin, Germany) acquired the synchronized PL decay to deduce the lifetime. Micro-absorption spectroscopy was performed by obtaining micro-reflection and micro-transmission spectra from the sample using a supercontinuum laser (FIU-6, NKT Photonics, Birkerød, Denmark).

Top-gated WS_2 devices were fabricated using a poly(methylmethacrylate) (PMMA; 950 A11, MicroChem)-assisted pick-and-place dry transfer method. Hexagonal boron nitride (hBN) (HQ Graphene) with ~ 50 – 100 nm thickness and monolayer graphene (HQ Graphene) were exfoliated from single crystal sources and used for the gate dielectric and electrodes, respectively. For gate voltage-dependent PL measurement, gate voltages were applied with a source meter (Model 2410, Keithley, Cleveland, OH, USA) through the top graphene electrode, while the WS_2 monolayer was electrically ground during measurement.

3. Results and Discussion

We applied two chemical doping methods for surface charge transfer onto the WS_2 monolayer, which are BV and K doping. Figure 1a illustrates the BV doping process, where the neutral BV molecule donates electrons to an acceptor material, which is monolayer WS_2 in this case. Since the BV possesses significantly low reduction potentials, n-doping is enabled and maintained under ambient conditions [16]. Figure 1b describes the process of K doping. When the K vapor is deposited onto the the WS_2 monolayer, the small electron affinity of K yields the transfer of electrons from K to WS_2 , achieving n-doping in the monolayer semiconductor.

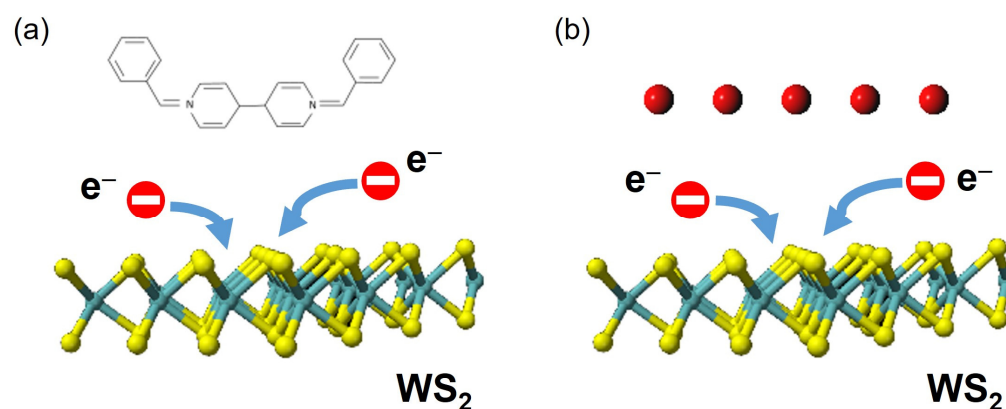


Figure 1. Schematic describing the n-doping procedure of the WS_2 monolayer with (a) a BV molecule and (b) K vapor. (Sulfur atoms: yellow, Tungsten atoms: cyan).

3.1. BV-Doped 2D Monolayer Semiconductor

In order to estimate the effectiveness of n-doping with BV, we fabricated an FET based on the WS₂ monolayer and measured its transfer characteristics. Figure 2a shows an optical micrograph of the fabricated WS₂ monolayer FET and Figure 2b illustrates the device structure where the gate voltage is applied through the backgate of the SiO₂/p+-Si substrate. In Figure 2c, the I_d - V_g transfer curves of the monolayer WS₂ FET are provided with respect to BV doping durations. Here, the device was immersed into the BV solution for controlled times and dried under N₂ prior to measurement. The as-fabricated monolayer WS₂ FET exhibits an ambipolar characteristic with both electron and hole conduction, determined by applied gate bias. Upon BV doping, the transfer curves of the device start to change significantly, with its electron conduction drastically increasing with a threshold voltage shift toward a more negative voltage. After 600 s of BV doping, the on-current level increases more than an order of magnitude, and only a small gate control over I_d is observed, indicating a strong doping effect by BV molecules. The electron concentration after BV doping in the WS₂ monolayer can be calculated from the equation:

$$n_{2D} = \frac{I_d L}{q W V_d \mu} \quad (1)$$

where n_{2D} is a carrier density in a 2D sheet, L is the channel length, q is the elementary charge, W is the channel width, and μ is the field-effect mobility. From the transfer curve, we obtained the field-effect mobility of $\mu = 26.1 \text{ cm}^2\text{V}^{-1}\text{s}^{-1}$ and thus the 2D electron density of $n_{2D} = 3.79 \times 10^{13} \pm 8.18 \times 10^{14} \text{ cm}^{-2}$.

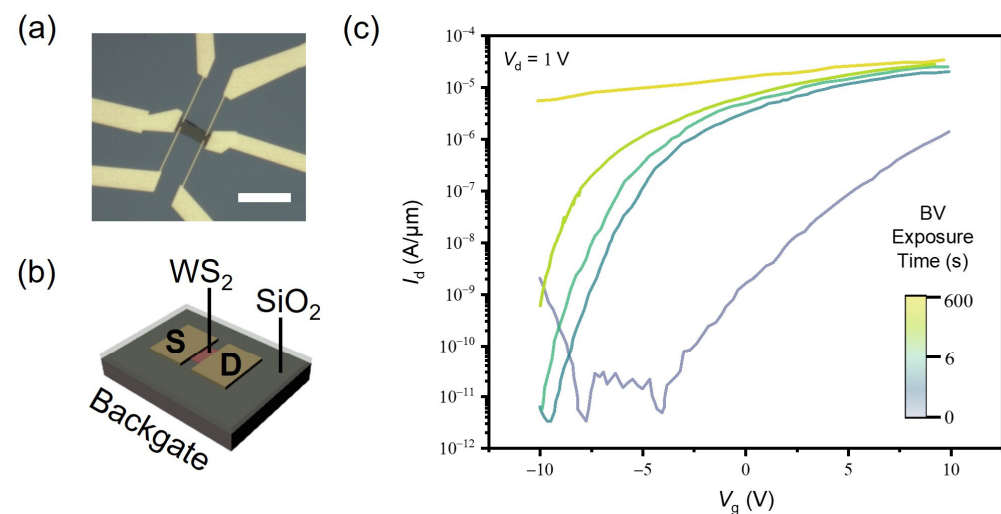


Figure 2. (a) Optical microscope images of the WS₂ monolayer FET. The scale bar is 20 μm . (b) Schematic of the FET device structure with a p+-Si backgate electrode and a 50 nm SiO₂ gate dielectric. (c) I_d - V_g transfer curves of the monolayer WS₂ FET at $V_d = 1 \text{ V}$ with increasing BV doping times.

3.2. Potassium-Doped 2D Monolayer Semiconductor

Doping the WS₂ monolayer with K results in strong n-type surface charge transfer doping. Owing to its reduction potential of -2.93 V , K doping has been used for improving contact resistance, which often restricts the performance of electronic devices [17]. To evaluate the doping effect with K, we fabricated a backgated FET, as shown in Figure 3a,b. In contrast with BV-doped WS₂ devices, the devices were measured under vacuum conditions as air exposure diminishes the doping effect due to the oxidation of K. In Figure 3c, it is shown that the I_d - V_g curve changes drastically as soon as the WS₂ monolayer is exposed to K vapor, which is why only a small dynamic range of K exposure time was covered in this experiment. After K doping, the I_d lost gate voltage dependence and the on-

current level increased more than orders of magnitude, exhibiting a clear consequence of degenerate n-doping. Similarly to the BV-doped WS₂ monolayer, the 2D electron density of $n_{2D} = 6.21 \times 10^{13} \pm 5.74 \times 10^{14} \text{ cm}^{-2}$ was calculated, which is higher than the value obtained for the same material but with BV doping and corresponds to the degenerate limit. This high electron concentration after K doping shows that there will be surface-dominant electronic transport, which can vary significantly with the different layer numbers of WS₂.

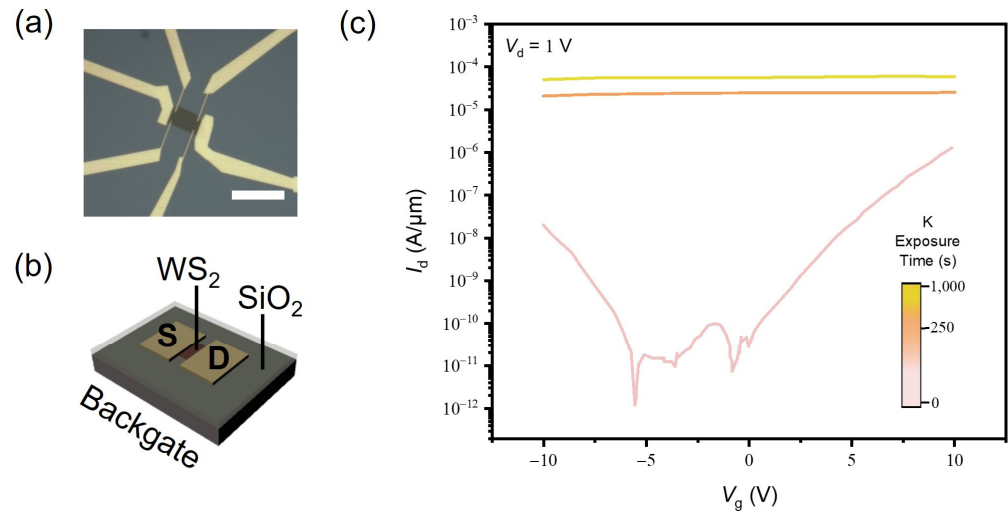


Figure 3. (a) Optical microscope images of the WS₂ monolayer FET. The scale bar is 20 μm. (b) Schematic of the FET device structure with a p+-Si backgate electrode and a 50 nm SiO₂ gate dielectric. (c) I_d - V_g transfer curves of the monolayer WS₂ FET at $V_d = 1 \text{ V}$ with increasing K doping times.

3.3. Luminescence Properties of the Chemically Doped 2D Monolayer Semiconductor

Next, we characterized the optical properties of BV- and K-doped WS₂ monolayers. We first analyzed the PL of the WS₂ monolayer as a function of BV doping time. In Figure 4a, the decreasing behaviors of PL intensity are observed with increasing BV doping durations. The PL intensity decrease with increasing BV doping is attributed to the increase in trion populations in the WS₂ monolayer. The recombination kinetics in the WS₂ monolayer is depicted using the following equation:

$$G = \frac{n_X}{\tau_X} + \frac{n_T}{\tau_T} + C_{bX}n_X^2 \quad (2)$$

where G is the generation rate of excitons, n_X and n_T are the neutral exciton and trion concentrations, respectively, τ_X and τ_T are the neutral exciton and trion lifetimes, respectively, and C_{bX} is the biexciton annihilation coefficient [27]. Then, PL QY is determined based on the equation below:

$$\text{PL QY} = \frac{1}{G} \left(\frac{n_X}{\tau_X} + \frac{n_T}{\tau_T} \right) \quad (3)$$

This provides us with theoretical guidance on the generation and recombination rates of quasi-particles consisting of monolayer semiconductors. The relationship between a negative charge concentration (N), trion concentration, and free electron concentration (n_e) is described as $N = n_e + n_T$. In particular, when electrons are dominant in a monolayer semiconductor, this relationship further expands to the following equation:

$$n_T = \frac{Tn_X}{1 + Tn_X}N \quad (4)$$

where T is the trion formation coefficient. Unless the exciton concentration is extremely high, meaning $Tn_X \gg 1$, which is the case when the trion concentration becomes equivalent

to the negative charge concentration ($n_T \approx N$), free electrons transferred into a monolayer semiconductor by doping contribute to the negative trion formation with excitons. Because the radiative lifetime of trions in the WS₂ monolayer ($\tau_{Tr} = \sim 0.032 \mu\text{s}$) is about 300 times longer than the nonradiative lifetime of trions in the WS₂ monolayer ($\tau_{Tr, nr} = \sim 0.1 \text{ ns}$), this leads to a dramatic increase in the nonradiative recombination rate and thus the PL intensity decreases [27]. Figure 4b presents the Urbach tail of the WS₂ monolayer with different BV exposure times. The slope of Urbach tails remains the same for increasing BV exposure times, indicating that there is no evidence of additional defect states produced by BV doping.

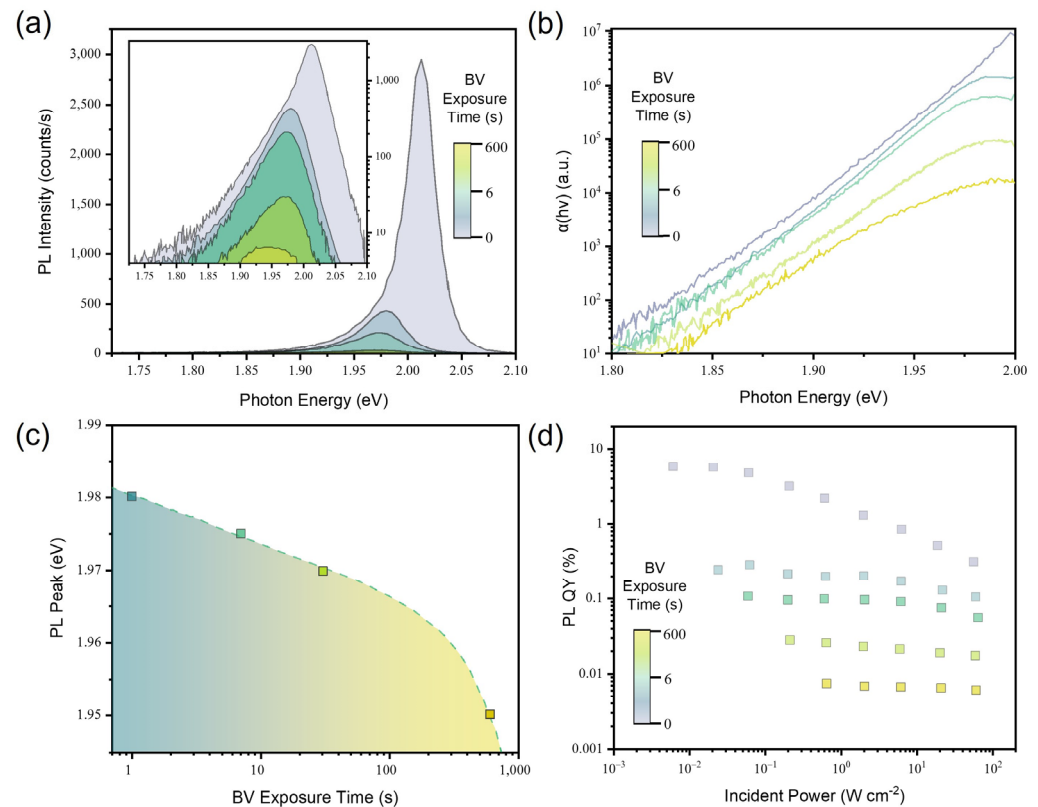


Figure 4. (a) PL spectra of the WS₂ monolayer measured at an incident power of 2 W/cm² with increasing BV exposure time. (b) The Urbach tail of the WS₂ monolayer as a function of BV exposure time. (c) The relationship between PL peak position and BV exposure times. (d) Incident power-dependent PL QY of the WS₂ monolayer with increasing BV exposure time.

The redshift of the PL emission spectra is observed with increasing BV doping times, as shown in Figure 4c. Given that the additional binding energy is required to form a trion from a neutral exciton, this result validates the PL intensity decrease which is associated with the increased trion population in the BV-doped WS₂ monolayer. Figure 4d shows the PL QY of the WS₂ monolayer after BV-doping at different amounts of time. We observed a monotonic decrease in the PL QY for all incident power ranges as the BV exposure time became longer, which is attributed to the high nonradiative recombination rates of trions.

Similarly, WS₂ monolayers with K doping were characterized by their PL emission spectra, as provided in Figure 5a. The same trend of decrease in PL intensity is observed in the WS₂ monolayer after K doping. In contrast to the BV-doped WS₂ monolayer, the neutral exciton emission peak remains and coexists with a trion emission peak when K doping is applied. This is possibly a consequence of a change in trion formation coefficient, triggered by strong binding between the K dopant and S plane in the lattice structure of WS₂ [17]. K doping does not bring about the introduction of defects or disorders which can act as recombination centers. As shown in Figure 5b, the preserved slope of Urbach tails

suggests that there is no lattice distortion or change in the density of states near the band edge upon K doping. With the increasing amount of K doping, the PL emission peak is shifted to a lower photon energy, owing to the increase in the trion population, as shown in Figure 5c. In the same way as BV doping, Figure 5d shows the decreased PL QY of the WS₂ monolayer after K doping. It should be noted that the maximum duration of BV and K doping is determined to the highest level possible within the range where the PL signal can still be distinguished from the background. In order to maximize the signal-to-noise ratio and widen the range of incident powers for evaluating the optical properties of BV- and K-doped WS₂ monolayers, the strategy to enhance light-matter interactions can be employed. For example, the introduction of nanostructures to increase outcoupling modes will enable a broader range of doping conditions and excitation powers. Furthermore, as a follow-up study, the altered photocarrier dynamics can also be examined upon the inclusion of nanostructures or nanoparticles based on free-carrier semiconductors [30,31].

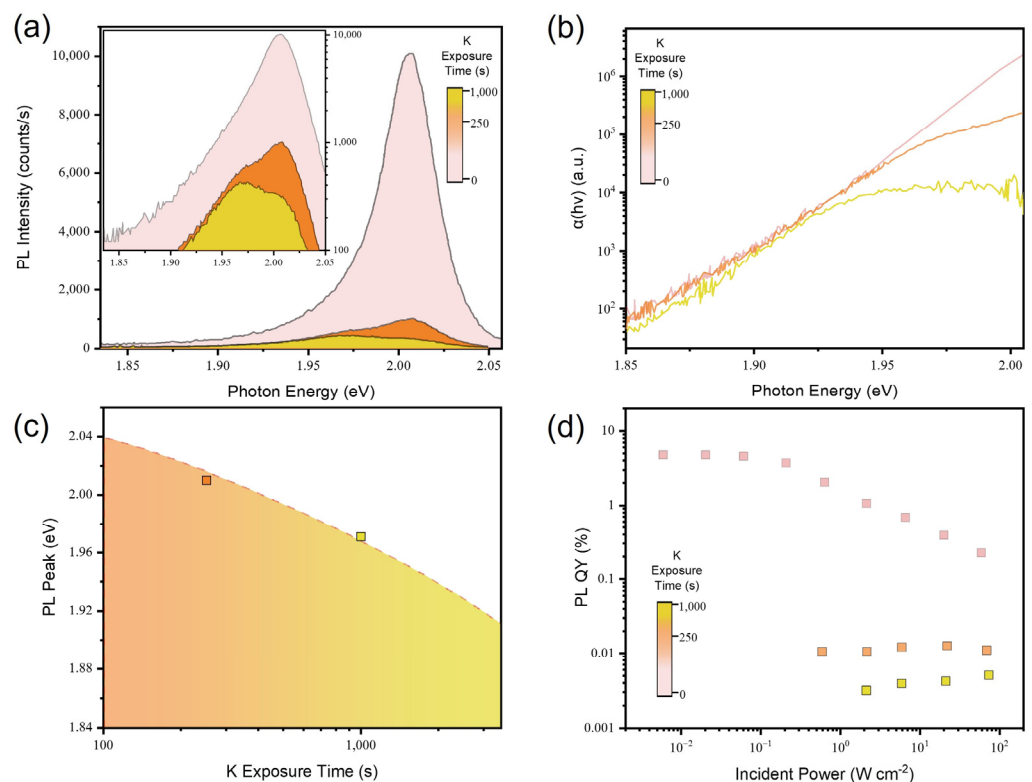


Figure 5. (a) PL spectra of the WS₂ monolayer measured at an incident power of 60 W/cm² with increasing K exposure time. (b) The Urbach tail of WS₂ monolayer as a function of K exposure time. (c) The relationship between PL peak position and K exposure time. (d) Incident power-dependent PL QY of the WS₂ monolayer with increasing K exposure time.

Moreover, dynamic luminescence behaviors were investigated for the WS₂ monolayer before and after BV doping. Figure 6a presents the time-resolved PL decay of a WS₂ monolayer to show the effect of BV doping on its recombination kinetics. Here, the radiative decay curves were fit by single exponential decay curves to extract lifetimes. As a result, the pristine WS₂ monolayer exhibits a luminescence lifetime of ~0.4 ns, which is consistent with a previous report [32]. The lifetime of the WS₂ monolayer then decreased to ~0.1 ns after 1000 s of BV exposure. Time-resolved PL measurements were performed with varying pump fluences, as shown in Figure 6b. At all pump fluences, it appears that BV doping shortens the lifetime of the WS₂ monolayer, arising from the fact that the luminescence decay is mainly dictated by the trion nonradiative recombination after BV doping to transfer the high density of electrons in the monolayer. It should be noted that the lifetime becomes shorter with increasing pump fluences owing to the exciton–exciton annihilation [27].

Photocarrier dynamics can also be evaluated using transient absorption spectroscopy, which enables one to capture the ultrafast decay of excited states. However, transient absorption spectroscopy requires higher pump intensity compared to time-resolved PL spectroscopy, limiting the dynamic range of measurement for recombination kinetics [33]. Figure 6c shows the absorption spectra of the pristine WS₂ monolayer in comparison with the WS₂ monolayer after 1000 s of BV exposure. While there was no measurable difference in terms of shapes and resonances between the two absorption spectra, the peak near the band edge of WS₂ shows ~30 meV redshift after BV doping. This is consistent with the PL shift induced by doping, which is associated with the trion formation from neutral excitons.

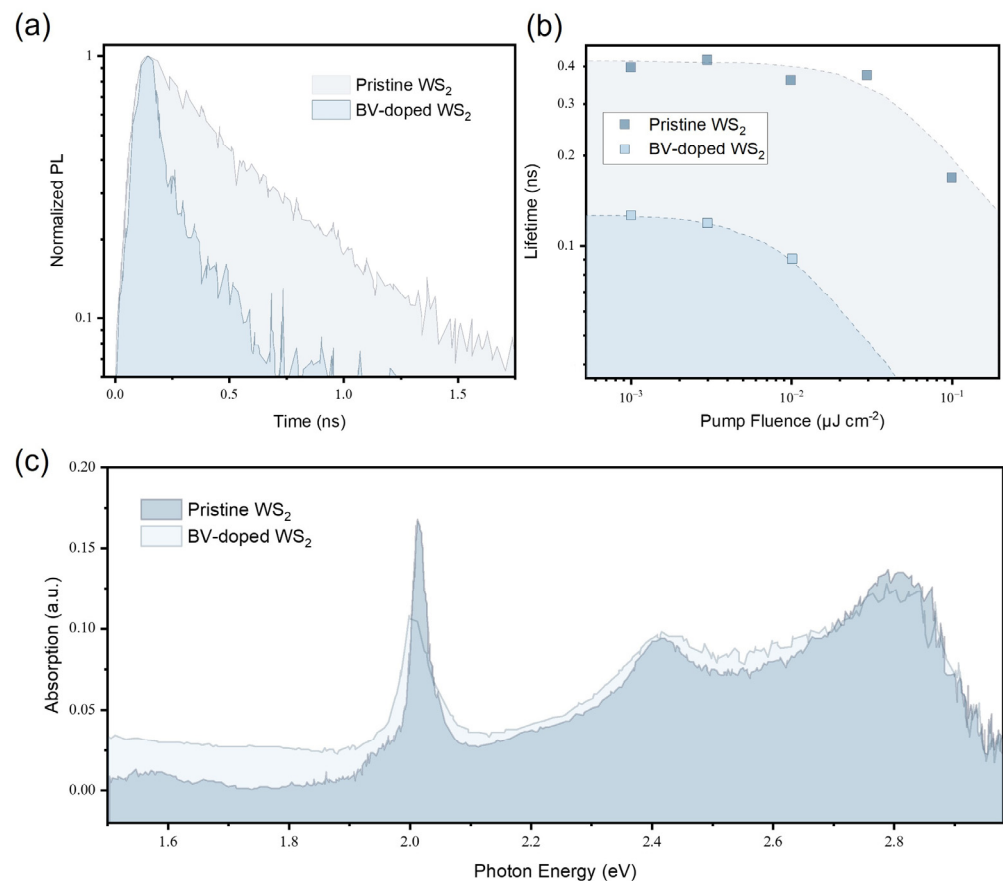


Figure 6. (a) Radiative decay of a pristine WS₂ monolayer and a doped-WS₂ monolayer with 1000 s of BV exposure. Time-resolved PL decay curves were acquired at a pump fluence of $3 \times 10^{-3} \mu\text{J}/\text{cm}^2$ (b) PL lifetime as a function of pump fluence for a pristine WS₂ monolayer and a doped-WS₂ monolayer with 1000 s of BV exposure. (c) Absorption spectra of a pristine WS₂ monolayer and a doped-WS₂ monolayer with 1000 s of BV exposure.

3.4. Luminescence Properties of the Electrically Doped 2D Monolayer Semiconductor

Besides the chemical doping methods, doping can also be achieved with electrostatic approaches. We evaluated the effectiveness of electrostatic doping by fabricating and characterizing a device where a gate voltage is applied with varying generation rates. Figure 7a displays a schematic of the two-terminal capacitor device structure with the top graphene as a gate electrode and the bottom graphene as a source electrode. Through simultaneous modulation of the gate voltage and generation rate, dominant recombination pathways in monolayer semiconductors are altered. As depicted in Figure 7b, at a negative V_g , electrons are taken away, and predominant recombination in the WS₂ monolayer becomes radiative due to neutral excitons. At a positive V_g , more electrons are injected into the WS₂ monolayer, leading to an increase in nonradiative recombination from negative trions. This gate voltage-dependent PL modulation of the WS₂ monolayer is measured

and provided in Figure 7c. As the applied gate voltage is modulated from a negative to positive bias, the higher concentration of trions formed from many electrons induces the PL intensity to decrease and the redshift of the PL spectrum, which coincides with the effect of chemical n-doping, such as BV and K. Here, the incident power (P) is converted into the exciton generation rate (G) according to the equation below:

$$G = \frac{\alpha P}{A \hbar \omega} \quad (5)$$

where α is the absorption at the excitation photon energy, A is the area of the laser spot, and $\hbar \omega$ is the excitation photon energy.

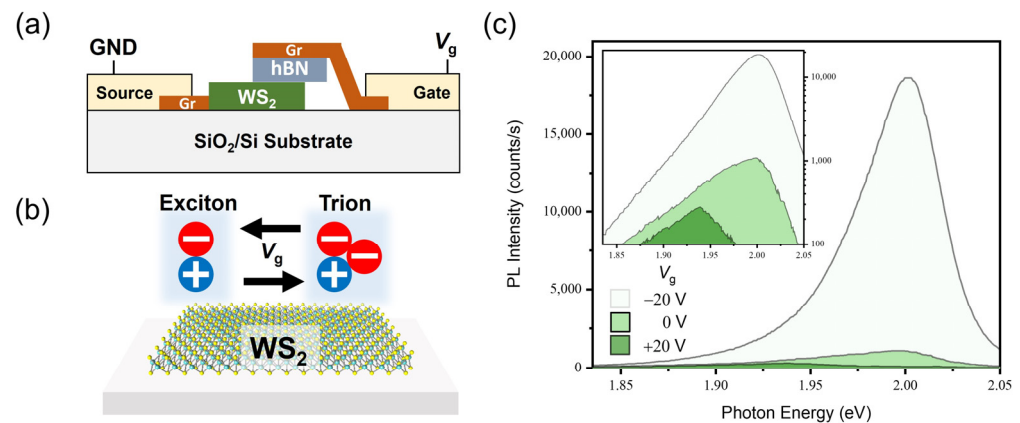


Figure 7. (a) Schematic describing the top-gated device structure. The top graphene layer acts as a gate electrode to apply electrostatic doping onto the WS₂ monolayer, while the bottom graphene is electrically ground. (b) Gate voltage-dependent modulation of PL in the WS₂ monolayer enabled by adjusting the exciton and trion density. (c) PL spectra of the WS₂ monolayer with gate voltages of $V_g = -20$ V, 0 V, and +20 V measured at an incident power of 1 W/cm².

Figure 8a shows the PL QY of the WS₂ monolayer measured under simultaneous variation of P and V_g . In the two-terminal capacitor device configuration, the total negative charge concentration (N) is calculated by the equation:

$$N = C_{OX} \frac{V_g - V_{th}}{q} \quad (6)$$

where V_{th} is the threshold voltage. Since the applied gate voltages adjust the total negative charge concentration (N) and the incident powers tune the generation rate (G), the free electron concentration (n_e) in the electrically-doped WS₂ monolayer can be extracted by numerically solving Equations (3) and (4) with substitution of the experimental parameters as well as the values for WS₂, including $\tau_{X_r} = 2$ ns, $\tau_{T_r} = 0.032$ μ s, $\tau_{T_{nr}} = 0.1$ ns, $T = 5 \times 10^{-12}$ cm², and $C_{bX} = 2.4$ cm²s⁻¹ reported in a previous work [27]. The free electron concentration of the WS₂ monolayer device at $V_g = 20$ V is therefore calculated as 3.12×10^{12} cm⁻².

The relationship between the maximum PL QY and the PL peak position of the WS₂ monolayer under electrostatic and chemical doping is presented in Figure 8b. This result suggests that both doping methods (Electrostatic and BV) cause plenty of free electron injection followed by trion formation, leading to the dominance of nonradiative recombination. It is shown that BV doping suppresses the PL QY of the WS₂ monolayer more significantly than electrostatic doping, curtailing the maximum PL QY by almost three orders of magnitude. This discrepancy between the two doping types originates from the fact that the free electron concentration of the BV-doped WS₂ monolayer is higher than the electrically-doped WS₂ monolayer. Moreover, it has been reported that the chemical

doping methods (BV and K) studied in this work are known to induce degenerate doping effects, lifting the Fermi level near to the conduction band edge [16,17].

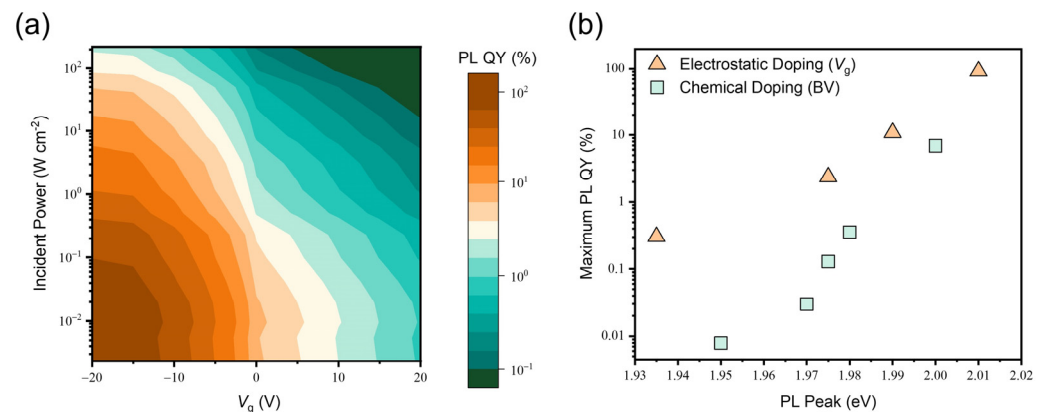


Figure 8. (a) PL QY of the WS₂ monolayer at different gate voltages and incident powers. (b) The relationship between the maximum PL QY and the PL peak position of the WS₂ monolayer after electrostatic and chemical doping.

4. Conclusion

In summary, the optical properties of an electrically doped WS₂ monolayer with surface charge transfer have been examined. BV doping and K doping both induce the PL spectra to be redshifted and the PL intensity to decrease, which is associated with the increased trion concentration. This is also supported by time-resolved PL and micro-absorption measurements. Based on the exciton and trion recombination model, the electron concentration of an electrically-doped WS₂ monolayer was extracted. The approach we took was to numerically solve the PL QY equation which is a function of the trion nonradiative recombination rate and the exciton radiative recombination rate at different generation rates.

In comparison with electrostatic doping, chemical doping methods such as BV and K doping cause degenerate doping in 2D TMDC monolayers. Therefore, further studies are required to unravel the correlation between the electrical parameters (electron concentration and mobility) and optical properties, especially for degenerately doped 2D monolayer semiconductors. Moreover, this work will provide opportunities for developing advanced doping technology, which can reversibly tune the exciton and trion density in 2D semiconductors.

Author Contributions: H.K., V.A. and S.-H.L. conceived the idea for the project and designed the experiment. H.K. and V.A. prepared the samples and performed the measurements. H.K., V.A. and S.-H.L. analyzed the data. H.K., V.A. and S.-H.L. wrote the manuscript. S.-H.L. supervised the project. All authors have read and agreed to the published version of the manuscript.

Funding: This work was supported by the National Research Foundation of Korea (NRF) grant funded by the Korean government (MSIT) (No. 2022M3H4A1A0409884213). This work was supported by the National R&D Program through the National Research Foundation of Korea (NRF) funded by the Ministry of Science and ICT (RS-2023-00277635). The authors appreciate the financial support from Samsung Advanced Institute of Technology.

Institutional Review Board Statement: Not applicable.

Informed Consent Statement: Not applicable.

Data Availability Statement: The data presented in this work are available upon request addressed to the corresponding author.

Conflicts of Interest: The authors declare no conflicts of interest.

References

1. Geim, A.K.; Grigorieva, I.V. Van der Waals heterostructures. *Nature* **2013**, *499*, 419–425. [[CrossRef](#)]
2. Mak, K.F.; Lee, C.; Hone, J.; Shan, J.; Heinz, T.F. Atomically thin MoS₂: A new direct-gap semiconductor. *Phys. Rev. Lett.* **2010**, *105*, 136805. [[CrossRef](#)] [[PubMed](#)]
3. Radisavljevic, B.; Radenovic, A.; Brivio, J.; Giacometti, V.; Kis, A. Single-layer MoS₂ transistors. *Nat. Nanotechnol.* **2011**, *6*, 147–150. [[CrossRef](#)] [[PubMed](#)]
4. Huang, X.; Zeng, Z.Y.; Zhang, H. Metal dichalcogenide nanosheets: Preparation, properties and applications. *Chem. Soc. Rev.* **2013**, *42*, 1934–1946. [[CrossRef](#)]
5. Kim, H.; Uddin, S.Z.; Lien, D.-H.; Yeh, M.; Azar, N.S.; Balendhran, S.; Kim, T.; Gupta, N.; Rho, Y.; Grigoropoulos, C.P.; et al. Actively variable-spectrum optoelectronics with black phosphorus. *Nature* **2021**, *596*, 232–237. [[CrossRef](#)] [[PubMed](#)]
6. Xia, F.; Wang, H.; Xiao, D.; Dubey, M.; Ramasubramanian, A. Two-dimensional material nanophotonics. *Nat. Photonics* **2014**, *8*, 899–907. [[CrossRef](#)]
7. Tongay, S.; Zhou, J.; Ataca, C.; Lo, K.; Matthews, T.S.; Li, J.; Grossman, J.C.; Wu, J. Thermally driven crossover from indirect toward direct bandgap in 2D semiconductors: MoSe₂ versus MoS₂. *Nano Lett.* **2012**, *12*, 5576–5580. [[CrossRef](#)]
8. Zhao, W.; Ghorannevis, Z.; Chu, L.; Toh, M.; Kloc, C.; Tan, P.; Goki, E. Evolution of electronic structure in thin sheets of WS₂ and WSe₂. *ACS Nano* **2013**, *7*, 791–797. [[CrossRef](#)]
9. Fang, H.; Chuang, S.; Chang, T.C.; Takei, K.; Takahashi, T.; Javey, A. High-performance single layered WSe₂ p-FETs with chemically doped contacts. *Nano Lett.* **2012**, *12*, 3788–3792. [[CrossRef](#)]
10. Chen, M.K.; Nam, H.; Wi, S.J.; Ji, L.; Ren, X.; Bian, L.F.; Lu, S.L.; Liang, X.G. Stable few-layer MoS₂ rectifying diodes formed by plasma-assisted doping. *Appl. Phys. Lett.* **2013**, *103*, 142110. [[CrossRef](#)]
11. Zhao, P.; Kiriya, D.; Azcatl, A.; Zhang, C.; Tosun, M.; Liu, Y.-S.; Hettick, M.; Kang, J.S.; McDonnell, S.; Kc, S.; et al. Air stable p-doping of WSe₂ by covalent functionalization. *ACS Nano* **2014**, *8*, 10808–10814. [[CrossRef](#)] [[PubMed](#)]
12. Bui, M.N.; Rost, S.; Auge, M.; Tu, J.-S.; Zhou, L.; Aguilera, I.; Blügel, S.; Ghorbani-Asl, M.; Krasheninnikov, A.V.; Hashemi, A.; et al. Low-energy Se ion implantation in MoS₂ monolayers. *NPJ 2D Mater. Appl.* **2022**, *6*, 42. [[CrossRef](#)]
13. Zhang, X.; Shao, Z.; Zhang, X.; He, Y.; Jie, J. Surface charge transfer doping of low-dimensional nanostructures toward high-performance nanodevices. *Adv. Mater.* **2016**, *28*, 10409–10442. [[CrossRef](#)] [[PubMed](#)]
14. Xiong, S.; Dai, Y.; Yang, J.; Xiao, W.; Li, D.; Liu, X.; Ding, L.; Gao, P.; Fahlman, M.; Bao, Q. Surface charge-transfer doping for highly efficient perovskite solar cells. *Nano Energy* **2021**, *79*, 105505. [[CrossRef](#)]
15. Xia, F.F.; Shao, Z.B.; He, Y.Y.; Wang, R.B.; Wu, X.F.; Jiang, T.H.; Duhm, S.; Zhao, J.W.; Lee, S.T.; Jie, J.S. Surface charge transfer doping *via* transition metal oxides for efficient p-type doping of II-VI nanostructures. *ACS Nano* **2016**, *10*, 10283–10293. [[CrossRef](#)] [[PubMed](#)]
16. Kiriya, D.; Tosun, M.; Zhao, P.; Kang, J.S.; Javey, A. Air-stable surface charge transfer doping of MoS₂ by benzyl viologen. *J. Am. Chem. Soc.* **2014**, *136*, 7853–7856. [[CrossRef](#)] [[PubMed](#)]
17. Fang, H.; Tosun, M.; Seol, G.; Chang, T.C.; Takei, K.; Javey, A. Degenerate n-doping of few-layer transition metal dichalcogenides by potassium. *Nano Lett.* **2013**, *13*, 1991–1995. [[CrossRef](#)] [[PubMed](#)]
18. Xiong, W.; Xia, C.; Du, J.; Wang, T.; Peng, Y.; Wei, Z.; Li, J. Band engineering of the MoS₂/Stanene heterostructure: Strain and electrostatic gating. *Nanotechnology* **2017**, *28*, 195702. [[CrossRef](#)] [[PubMed](#)]
19. Robbins, M.C.; Koester, S.J. Black phosphorus p- and n-MOSFETs with electrostatically doped contacts. *IEEE Electron Device Lett.* **2017**, *38*, 285–288. [[CrossRef](#)]
20. Liao, F.; Sheng, Y.; Guo, Z.; Tang, H.; Wang, Y.; Zong, L.; Chen, X.; Riaud, A.; Zhu, J.; Xie, Y.; et al. MoS₂ dual-gate transistors with electrostatically doped contacts. *Nano Res.* **2019**, *12*, 2515–2519. [[CrossRef](#)]
21. Wang, Q.H.; Kalantar-Zadeh, K.; Kis, A.; Coleman, J.N.; Strano, M.S. Electronics and optoelectronics of two-dimensional transition metal dichalcogenides. *Nat. Nanotechnol.* **2012**, *7*, 699–712. [[CrossRef](#)] [[PubMed](#)]
22. Tan, C.; Cao, X.; Wu, X.J.; He, Q.; Yang, J.; Zhang, X.; Chen, J.; Zhao, W.; Han, S.; Nam, G.-H.; et al. Recent advances in ultrathin two-dimensional nanomaterials. *Chem. Rev.* **2017**, *117*, 6225–6331. [[CrossRef](#)]
23. Chaves, A.; Azadani, J.; Alsalman, H.; Da Costa, D.; Frisenda, R.; Chaves, A.; Song, S.H.; Kim, Y.; He, D.; Zhou, J.; et al. Bandgap engineering of two-dimensional semiconductor materials. *NPJ 2D Mater. Appl.* **2020**, *4*, 29. [[CrossRef](#)]
24. Amani, M.; Lien, D.-H.; Kiriya, D.; Xiao, J.; Azcatl, A.; Noh, J.; Madhupathy, S.R.; Addou, R.; KC, S.; Dubey, M.; et al. Near-unity photoluminescence quantum yield in MoS₂. *Science* **2015**, *350*, 1065–1068. [[CrossRef](#)] [[PubMed](#)]
25. Kim, H.; Lien, D.H.; Amani, M.; Ager, J.W.; Javey, A. Highly stable near-unity photoluminescence yield in monolayer MoS₂ by fluoropolymer encapsulation and superacid treatment. *ACS Nano* **2017**, *11*, 5179–5185. [[CrossRef](#)] [[PubMed](#)]
26. Uddin, S.Z.; Kim, H.; Lorenzon, M.; Yeh, M.; Lien, D.H.; Barnard, E.S.; Htoon, H.; Weber-Bargioni, A.; Javey, A. Neutral exciton diffusion in monolayer MoS₂. *ACS Nano* **2020**, *14*, 13433–13440. [[CrossRef](#)] [[PubMed](#)]
27. Lien, D.-H.; Uddin, S.Z.; Yeh, M.; Amani, M.; Kim, H.; Ager, J.W.; Yablonovitch, E.; Javey, A. Electrical suppression of all nonradiative recombination pathways in monolayer semiconductors. *Science* **2019**, *364*, 468–471. [[CrossRef](#)] [[PubMed](#)]
28. Kim, H.; Uddin, S.Z.; Higashitarumizu, N.; Rabani, E.; Javey, A. Inhibited nonradiative decay at all exciton densities in monolayer semiconductors. *Science* **2021**, *373*, 448–452. [[CrossRef](#)] [[PubMed](#)]
29. Uddin, S.Z.; Higashitarumizu, N.; Kim, H.; Rabani, E.; Javey, A. Engineering exciton recombination pathways in bilayer WSe₂ for bright luminescence. *ACS Nano* **2022**, *16*, 1339–1345. [[CrossRef](#)]

30. Gyawali, S.; Tirumala, R.T.; Loh, H.; Andiappan, M.; Bristow, A.D. Photocarrier recombination dynamics in highly scattering Cu₂O nanocatalyst clusters. *J. Phys. Chem. C* **2024**, *128*, 2003–2011. [[CrossRef](#)]
31. Yan, J.; Ma, C.; Huang, Y.; Yang, G. Tunable control of interlayer excitons in WS₂/MoS₂ heterostructures via strong coupling with enhanced Mie resonances. *Adv. Sci.* **2019**, *6*, 1802092. [[CrossRef](#)] [[PubMed](#)]
32. Amani, M.; Taheri, P.; Addou, R.; Ahn, G.H.; Kiriya, D.; Lien, D.-H.; Ager, J.W.; Wallace, R.M.; Javey, A. Recombination kinetics and effects of superacid treatment in sulfur- and selenium-based transition metal dichalcogenides. *Nano Lett.* **2016**, *16*, 2786–2791. [[CrossRef](#)] [[PubMed](#)]
33. Gyawali, S.; Tirumala, R.T.A.; Andiappan, M.; Bristow, A.D. Carrier dynamics in cuprous oxide-based nanoparticles and heterojunctions. In Proceedings of the SPIE. Ultrafast Phenomena and Nanophotonics XXVIII, San Francisco, CA, USA, 29–31 January 2024; Volume 12884, pp. 73–79.

Disclaimer/Publisher’s Note: The statements, opinions and data contained in all publications are solely those of the individual author(s) and contributor(s) and not of MDPI and/or the editor(s). MDPI and/or the editor(s) disclaim responsibility for any injury to people or property resulting from any ideas, methods, instructions or products referred to in the content.